

Open Research Online

The Open University's repository of research publications and other research outputs

Chemical analysis of trace elements at the nanoscale in samples recovered from laser-heated diamond anvil cell experiments

Journal Item

How to cite:

Blanchard, Ingrid; Petitgirard, Sylvain; Laurenz, Vera; Miyajima, Nobuyoshi; Wilke, Max; Rubie, David C.; Lobanov, Sergey S.; Hennet, Louis; Morgenroth, Wolfgang; Tucoulou, Rémi; Bonino, Valentina; Zhao, Xuchao and Franchi, Ian (2022). Chemical analysis of trace elements at the nanoscale in samples recovered from laser-heated diamond anvil cell experiments. *Physics and Chemistry of Minerals*, 49(6) p. 18.

For guidance on citations see [FAQs](#).

© 2022 The Authors



<https://creativecommons.org/licenses/by-nc-nd/4.0/>

Version: Version of Record

Link(s) to article on publisher's website:

<http://dx.doi.org/doi:10.1007/s00269-022-01193-7>

Copyright and Moral Rights for the articles on this site are retained by the individual authors and/or other copyright owners. For more information on Open Research Online's data [policy](#) on reuse of materials please consult the policies page.



Chemical analysis of trace elements at the nanoscale in samples recovered from laser-heated diamond anvil cell experiments

Ingrid Blanchard^{1,3} · Sylvain Petitgirard^{2,3} · Vera Laurenz³ · Nobuyoshi Miyajima³ · Max Wilke¹ · David C. Rubie³ · Sergey S. Lobanov⁴ · Louis Hennet⁵ · Wolfgang Morgenroth^{1,6} · Rémi Tucoulou⁶ · Valentina Bonino⁶ · Xuchao Zhao⁷ · Ian Franchi⁷

Received: 9 January 2022 / Accepted: 7 April 2022
© The Author(s) 2022

Abstract

High pressure and high temperature experiments performed with laser-heated diamond anvil cells (LH-DAC) are being extensively used in geosciences to study matter at conditions prevailing in planetary interiors. Due to the size of the apparatus itself, the samples that are produced are extremely small, on the order of few tens of micrometers. There are several ways to analyze the samples and extract physical, chemical or structural information, using either in situ or ex situ methods. In this paper, we compare two nanoprobe techniques, namely nano-XRF and NanoSIMS, that can be used to analyze recovered samples synthesized in a LH-DAC. With these techniques, it is possible to extract the spatial distribution of chemical elements in the samples. We show the results for several standards and discuss the importance of proper calibration for the acquisition of quantifiable results. We used these two nanoprobe techniques to retrieve elemental ratios of dilute species (few tens of ppm) in quenched experimental molten samples relevant for the formation of the iron-rich core of the Earth. We finally discuss the applications of such probes to constrain the partitioning of trace elements between metal and silicate phases, with a focus on moderately siderophile elements, tungsten and molybdenum.

Keywords NanoSIMS · Nano-XRF · Diamond anvil cell · Focused ion beam

This article is part of a Topical Collection “Experimental and Analytical Techniques at Extreme and Ambient Conditions”, guest edited by Stella Chariton, Vitali B. Prakapenka and Haozhe (Arthur) Liu.

✉ Ingrid Blanchard
blanchard@uni-potsdam.de

✉ Sylvain Petitgirard
sylvain.petitgirard@erdw.ethz.ch

¹ Institut für Geowissenschaften, Universität Potsdam,
14476 Potsdam, Germany

² ETH Zürich, 8092 Zurich, Switzerland

³ Bayerisches Geoinstitut, Universität Bayreuth,
95440 Bayreuth, Germany

⁴ GFZ German Research Centre for Geosciences,
Telegrafenberg, 14473 Potsdam, Germany

⁵ ICMN, CNRS and University of Orleans, 45071 Orléans,
France

⁶ ESRF-The European Synchrotron, 38043 Grenoble, France

⁷ School of Physical Sciences, Open University,
Milton Keynes MK7 6AA, UK

Introduction

It has long been established that most of the composition of Earth’s main reservoirs (i.e. the core and the bulk silicate Earth) is the result of thermodynamic equilibrium at high pressures (P) and temperatures (T) during the accretion and differentiation of the planet, about 4.5 billion years ago (see a review by Rubie et al. 2015b). During the accretion stage, collisions between Mars-sized embryos and proto-planets are sufficiently energetic to partially or fully melt the planet. This resulted in a succession of deep magma oceans that led to the chemical fractionation of siderophile elements (iron-loving elements) and lithophile elements (silicate-loving elements) between the different reservoirs. The major element compositions of the mantle and the core of the planet were fixed once the accretion and differentiation of the planet were finished, about 200 million years after the beginning of solar system history. The chemical compositions of Earth’s reservoirs have direct implications for countless properties of the Earth, such as its internal dynamics, through its magnetic field produced in the core, and mantle convection, or

habitability at the surface. To understand the observables that we have today, it is necessary to simulate in the laboratory the conditions of Earth's formation.

The most commonly-used static tool to generate the pressure and temperature conditions of Earth's differentiation ($P > 40$ GPa, $T > 3500$ K) simultaneously is the laser-heated diamond anvil cell apparatus (LH-DAC), although recent developments have enabled high P – T conditions to be achieved using internal resistive heating in the diamond anvil cell (Heinen et al. 2021), which minimizes the thermal gradient in such experiment. The LH-DAC can be combined with different in situ techniques to monitor the changes in structure or composition that are induced by elevated P – T compositions. Among other techniques, the most prominent ones include X-ray diffraction, X-ray fluorescence and absorption spectroscopy and X-ray imaging, which can be performed in situ under high P – T conditions using synchrotron radiation, as reviewed by Shen and Mao (2017). In addition to, or apart from, in situ measurements performed whilst the sample is at high P (and sometimes high T), it is also possible to perform ex situ analysis of the sample after high temperature and pressure conditions are released. Analyzing quenched samples ex situ has been performed previously after preparation by the Focused Ion Beam (FIB) technique (e.g. Irifune et al. 2005; Miyahara et al. 2008; Ricolleau et al. 2008; Fiquet et al. 2010; Siebert et al. 2012; Blanchard et al. 2017; Jackson et al. 2018). The FIB has thus become the most commonly used technique to extract a lamella of a sample synthesized in a LH-DAC. Further chemical characterization can then be performed using electron microprobe (EPMA), and after further thinning, transmission electron microscopy (TEM). Those techniques present different advantages and disadvantages, but most importantly they are only suitable to quantify element concentrations in excess of the several hundred ppm level, and only if appropriate standards are available.

Understanding the distribution of trace elements between Earth's reservoirs is essential to place constraints on the different steps of the accretion. Siderophile elements present in trace concentrations in the Earth's mantle can provide important information on the conditions of Earth's differentiation. For example, the redox environment of the early Earth can be constrained using vanadium (e.g. Siebert et al. 2013) or the depth of the magma ocean using nickel and cobalt (Li and Agee 1996; Bouhifd and Jephcoat 2011; Siebert et al. 2012). Ultimately, the results of such experiments with multiple elements can be combined to build self-consistent models of Earth's accretion and differentiation (e.g. Rubie et al. 2015a).

In high P – T experiments, the elements of interest are usually doped at higher level in the starting material compared to their natural abundances to ensure concentrations that are detectable by EPMA in both the metallic and the silicate

phase. Highly siderophile elements (HSE) are present in the Bulk Silicate Earth (BSE) in chondritic proportions (Kimura et al. 1974; Chou et al. 1983). This is at odds with their strong affinity for iron, which should have led to a complete segregation of these elements into the core during Earth's accretion. This observation has been the basis of a late stage of meteoritic bombardment on Earth after the core formation ceased, to explain HSEs abundances in the mantle. Up to about 0.5% of Earth's mass would have been accreted during this episode (Walker 2009; Rubie et al. 2016) to explain the abundances of these element in the mantle. Studying the partitioning of these siderophile elements between metal and silicate at the possible conditions of core formation ($P > 40$ GPa and $T > 3500$ K) is of fundamental importance, but analyzing trace element concentrations in quenched silicate melts produced in the LH-DAC is far from easy. For LH-DAC experiments, the sample is contained in a sample chamber of a metallic gasket of about 100 μm in diameter, and 25 μm thickness (both depending greatly on the pressure), and the final heated area is about 20 μm in diameter. As described above, the samples are usually extracted using FIB, which results in sample dimensions of about $20 \times 20 \times 3$ microns (length \times width \times thickness). In that case, classical techniques used for samples synthesized with large volume presses such as laser ablation ICPMS cannot be used to detect trace element abundances (e.g. Mann et al. 2012; Laurenz et al. 2016). Therefore, the use of special techniques that include microfabrication using a FIB to extract a lamella of the sample at a very precise location has become of great importance and is described later in this manuscript.

In this report, we will describe and compare two different methods that allow the determination of elemental concentrations in standard samples and elemental ratios in recovered samples from high-pressure experiments, namely Nanoscale secondary ion mass spectrometry (NanoSIMS) and synchrotron radiation nano X-ray fluorescence (nano-XRF). Both methods have been used already by the high P – T Earth science community. Badro et al. (2007) proposed to use NanoSIMS to study the partitioning of elements (strontium, scandium and yttrium) between the different phases of Earth's lower mantle present at very low concentration (few tens of ppm). Recently, NanoSIMS was used to investigate the metal–silicate partitioning of carbon and platinum (Fischer et al. 2020; Suer et al. 2021; Blanchard et al. 2022) in the context of Earth's core–mantle differentiation. XRF has also been used previously with LH-DAC techniques (Andraut et al. 2012; Petitgirard et al. 2012), but only in situ, and not with a nanometer-sized beam as discussed here, but with a micrometer-sized beam. NanoSIMS and nano-XRF techniques are very different in various aspects, the most important being that nano-XRF is a deeply penetrative but nondestructive method, whereas NanoSIMS is a surface sensitive and destructive method. The second

major difference between the two techniques is that NanoSIMS can probe isotopes, whereas nano-XRF cannot. We will especially focus on the use of these techniques to measure various siderophile elements (from moderately to highly siderophile, hereafter MSE and HSE, respectively) present in trace amounts in quenched silicate melts, and at a few wt% level in metallic alloys. We will first present our results on several kinds of standards, before moving on to samples synthesized at high *P–T* conditions in a LH-DAC.

Methods and results for standards

Synthesis and preparation of standards

Before measuring actual samples from LH-DAC, it is necessary to have appropriate standards, with known composition in both major and trace elements. Suitable standards are a key for both nanoprobe techniques presented here. We have synthesized standards using an aerodynamic levitation furnace (Auzende et al. 2011) for MSEs. We also used a glass synthesized with a piston cylinder press and described elsewhere (Chen et al. 2020) for HSEs. An aerodynamic levitation furnace enables homogeneous glasses to be synthesized

that are doped in the element(s) of interest, and has already been used and presented in previous publications related to high *P–T* experiments (e.g. Blanchard et al. 2017). Here, we have used this technique to synthesize silicate glasses and metals doped in molybdenum and tungsten (Mo and W) at the CEMHTI laboratory in Orléans, France. For the silicate, we started by mixing high purity oxide and carbonate powders in an agate mortar to reproduce the composition of the primitive upper mantle in major elements as determined by Palme and O'Neill (2014). We added WO₃ and MoO₃ in different proportions (see Table 1). The powder samples were subsequently decarbonated, pressed into small pellets of about 25 mg and placed in the nozzle of the aerodynamic levitation furnace. A CO₂ laser is then focused on the sample and, as it melts, the gas flow is increased to maintain the levitation of the liquid in the conical nozzle. The melting is detected via a temperature plateau using a pyrometer, and a stable levitation is monitored through a video system. After few seconds of melting, the power of the laser is cut off to immediately quench the sample into a glass. The synthesized spheres were then cut in half and polished to perform chemical analysis. We analyzed major elements using EPMA, and trace elements by both LA-ICP-MS and EPMA at the Bayerisches Geoinstitut (BGI, Bayreuth, Germany). Both methods

Table 1 Compositions of the silicate standards and starting material along with their respective uncertainties used in this study reported in wt% except when indicated differently

	PO1	<i>σ</i> PO1	PO0.5	<i>σ</i> PO0.5	PO1000	<i>σ</i> PO1000	PO100	<i>σ</i> PO100	IZ-01	<i>σ</i> IZ
SiO ₂	46.44	0.18	47.38	0.19	48.91	0.21	49.58	0.16	49.1	0.4
MgO	33.50	0.13	32.24	0.21	32.53	0.19	32.17	0.24	10.0	0.6
FeO	8.32	0.08	9.00	0.09	9.21	0.09	9.28	0.10	0.19	0.05
CaO	3.99	0.14	4.20	0.19	3.87	0.18	3.79	0.10	22.6	0.4
Al ₂ O ₃	4.71	0.04	4.82	0.05	4.16	0.04	3.90	0.06	14.8	0.8
MnO	0.16	0.04	0.20	0.04	0.18	0.03	0.17	0.03	–	–
TiO ₂	0.17	0.01	0.23	0.01	0.22	0.02	0.21	0.02	0.22	0.04
Cr ₂ O ₃	0.30	0.02	0.35	0.02	0.39	0.02	0.41	0.02	–	–
^a WO ₃	0.948		0.495		0.100		0.0097		–	–
^b WO ₃	1.041	0.09	0.552	0.07	0.103	0.04	0.0330	0.04	–	–
^a MoO ₃	0.768		0.417		0.086		0.0095		–	–
^b MoO ₃	0.798	0.03	0.46	0.03	0.086	0.02	0.0070	0.009	–	–
Re (ppm)	–		–		–		–		1198	0.6
Pd (ppm)	–		–		–		–		45	1.1
Rh (ppm)	–		–		–		–		65	0.4
Ru (ppm)	–		–		–		–		994	0.4
Ag (ppm)	–		–		–		–		1231	1.5
Ir (ppm)	–		–		–		–		423	0.9
Pt (ppm)	–		–		–		–		4385	0.9
Au (ppm)	–		–		–		–		0.6	6.8
Total ^c	99.43	0.35	99.43	0.43	99.67	0.37	99.54	0.32		

Standard IZ-01 is from Chen et al. (2020)

The numbers in italics are the uncertainties associated with each measurements

^aValues obtained by LA-ICP-MS

^bValues obtained by EPMA

^cTotal calculated for EPMA measurements

show similar results for standards containing up to 1000 ppm of Mo or W, but diverge for standards containing 100 ppm, with LA-ICP-MS values much closer to the expected concentrations. Using those methods, we could demonstrate that the standards were homogeneous over their entire volume. We report in Table 1 the compositions of the standards synthesized by this method. During levitation, the gas composition can be changed, which influences the redox environment of the sample. For silicate standards, we used an argon flux, allowing to maintain reducing conditions. Likewise, spheres of metal Fe doped in W and Mo were synthesized by aerodynamic levitation in purified argon to be used as standards. We synthesized three different metallic standards with various concentrations of W and Mo to establish calibration curves of the nanoprobe against the reference analysis using the microprobe and LA-ICP-MS. The compositions of the metallic spheres were checked using EPMA at BGI and are reported in Table 2.

For HSEs, we have used a standard synthesized in a piston cylinder apparatus to create homogeneous glasses doped in siderophile elements by Chen et al. (2020). A complication with HSEs in silicate glasses that was noted previously (Brenan et al. 2003; Ertel et al. 2008; Médard et al. 2015) is the occurrence of metallic nanonuggets. The problem is to consider those nuggets as either quench products, or a stable equilibrium phase at the experimental conditions. Médard et al. (2015) demonstrated that nanonuggets were experimental artifacts formed during the quench, and hence should be avoided when analysing HSE concentrations in silicate glass in order not to overestimate their abundances. The glass used here contained several HSEs and was carefully checked at high resolution by Chen et al. (2020). Their analysis did not reveal any metal nanonuggets within a resolution of about 10 nm. We report in Table 1 the composition of this standard (IZ-01) for which the details of preparation can be found in Chen et al. (2020). This standard offers a wide diversity of siderophile elements (Ag, Pd, Rh, Ru, Pt, Ir, Au and Re) at different concentrations, from tens to thousands of ppm. In the following, we have especially worked on the elements Ag, Rh, Ru and Re using this standard.

Since nano-XRF is a penetrative method, we wanted to assess the importance of the geometry of the experimental set-up on the measurements, so we have performed several tests. We have tested keeping the standards as a bulk

(few millimeters) and also extracted lamellae with different thicknesses using a Ga⁺ beam FIB at the BGI and at the GFZ (Potsdam, Germany). Details of the FIB procedure are described in the supplementary information and are also discussed in length in Lemelle et al. (2017).

Nano-XRF measurements

Nano-XRF measurements were performed on the ID16B beamline at the European Synchrotron Radiation Facility (ESRF, France). This beamline is dedicated to hard X-ray nano-analysis with a spatial resolution of $59 \times 44 \text{ nm}^2$ and can reach very high flux ($10^{12} \text{ photons s}^{-1}$) using a pink beam ($\Delta E/E = 10^{-2}$) mode (quasi-monochromatic), considerably reducing the acquisition time per analyzed points. The X-ray beam was set at 29.5 keV, and the brilliance was very high with a maximum photon flux of $1.4 \times 10^{12} \text{ photons s}^{-1}$ at the sample location. During the experiment, X-ray photons shine on the samples ejecting core electrons from atomic orbitals. The created holes are then filled by electrons from higher orbitals. During this relaxation process, X-ray photons (fluorescence photons) are re-emitted with characteristic energies for each element in the periodic table and are detected by solid state detectors to infer the elemental composition in the illuminated specimen area. The instrument is equipped with two multi-element Si-drift detectors with 3 and 7 elements, respectively (of 50 mm^2 active area each) positioned in a back-scattered geometry at approximately 15° from the sample plane that can work simultaneously to collect the maximum signal. Using this technique, it is possible to map a large area (up to 30×20 microns in our case) of our standards and samples with a high sensitivity for the heavy elements studied here. Using an excitation energy of 29.5 keV, we could reach the K-emission lines of Mo, Ag, Rh, Ru and the L-lines of W and Re. Attenuators in the incoming beam are used if needed, to avoid the saturation of the detectors and keep dead time below 30% (usually even below 15%), meaning that the fluorescence-photon events are counted as real and not electronically generated due to an excess photon that would saturate the detector. This low detector dead time can be accurately compensated by a simple linear correction. At such high energy the X-ray incident beam can penetrate millimeters of material and the XRF signal for different elements will be affected by the thickness

Table 2 Metal spheres used as standards with different concentrations of Mo and W, in wt%

	Met 1	$\sigma_{Met 1}$	Met 2	$\sigma_{Met 2}$	Met 3	$\sigma_{Met 3}$
Fe	88.5	<i>0.6</i>	96.8	<i>1.15</i>	98.9	<i>0.5</i>
W	3.3	<i>0.3</i>	0.27	<i>0.18</i>	–	–
Mo	4.8	<i>0.1</i>	1.2	<i>0.05</i>	0.45	<i>0.03</i>
Ni	5.00	<i>0.08</i>	4.24	<i>0.10</i>	3.21	<i>0.06</i>
Total	101.6	<i>0.6</i>	102.5	<i>1.12</i>	102.7	<i>0.5</i>

The numbers in italics are the uncertainties associated with each measurements

of the sample. High energy fluorescence (i.e., Mo K alpha, at 17.48 keV) can be generated at depth in the sample and find their way out, while lower energies fluorescence signals (i.e., Fe at 6.4 keV, Ca at 3.6 keV) will be strongly affected by self-absorption effect within the sample. Standards and samples extracted by FIB were mounted on Cu-grids during the FIB preparation, and each grid was subsequently taped to a Si₃N₄ membrane using double sided tape. The membrane itself was attached to a PEEK holder using Kapton tape. As developed in the following, we also tested the nano-XRF technique on bulk samples (i.e., not extracted by FIB).

Using the nano-XRF, we acquired high precision chemical distribution maps of the standards (500–1000 ms exposure time per pixel) with step sizes on the order of 100 nm from which we could extract Regions of Interest (ROIs). Each pixel represents one data point containing a full energy dispersive XRF-spectrum, so by summing up a large area, or ROI, the statistics of the sum spectrum is highly improved. In Fig. 1, we illustrate the effect of different geometries on nano-XRF measurements. Figure 1a and b highlight the differences in XRF intensities for Mo-line peak and Mo/Fe ratio, respectively as a function of the thickness of the FIB cut silicate standard. We compare 1-, 3- and 5- micron thick samples along with a large half sphere of the different materials synthesized with aerodynamic levitation. One can see on Fig. 1a that using the XRF peak intensity of Mo, the intensity is significantly lower for the 1-micron thick sample compared to the 5-micron thick one and also the estimated concentration of Mo in the standard increases with increasing thickness. Figure 1b highlights the importance of using XRF intensity ratios instead to establish calibration curves that are trustworthy, since in this case it circumvents the effect of thickness and we see no more difference between the different thicknesses for FIB extracted lamellae. We also compare in Fig. 1b the XRF intensity ratios of Mo/Fe for both the large spheres (“infinite thickness”) and the FIB foils, and it is clear that there is a strong difference in the intensity of the signal between the two. Thus, the sample and standard should have the same thickness within a few microns. This figure highlights the importance of having standards that have a geometry close to that of the sample itself to define the calibration curve. It also shows that using the aerodynamic levitation furnace is a great option to synthesize standards, since even at extremely small scales (well below 1 micron), the sample is homogeneous. A close up of the FIB-extracted samples presented in Fig. 1b is provided in Fig. S2c. In the two lower panels of Fig. 1, we compare the spectra obtained in the case of a FIB lamella (3-micron thickness) with the one obtained with a large sphere. One can see again that the counts are much higher in the second case. The difference in background in Fig. 1c and d is due to the presence of Cu and Pt contributions in Fig. 1c that changes the intensity in the range between 8 and 12 keV.

Additionally, the thickness also affects the noise level at high energy when comparing the Mo peak between the two samples. We present in Fig. S2 nano-XRF maps obtained for the different FIB thicknesses and for the sphere. The difference thicknesses were estimated from views from the top of the FIB lamellae during the FIB process.

Because the composition of the sample is known from our previous EPMA and/or LA-ICP-MS measurements, we could also retrieve the concentrations of several siderophile elements. To do so, we used the software PyMca developed at the ESRF (Solé et al. 2007). We defined one ROI in standard IZ-01 at the center of the FIB lamella and we defined the major elements that are known for the matrix, which includes also the light elements that are not detected in the XRF spectra (i.e., elements with Z lower than that of Na). With this information and using calcium as internal standard, a matrix correction could be performed (Beckhoff et al. 2007) and we could access the trace-element composition of the sample. We note that PyMca also accounts for secondary fluorescence by the matrix correction. It also takes into account the re-absorption of the XRF from the sample and of the air between sample and detector when all these parameters are known, i.e. sample thickness, distance between sample and detector and geometry of the sample and detector.

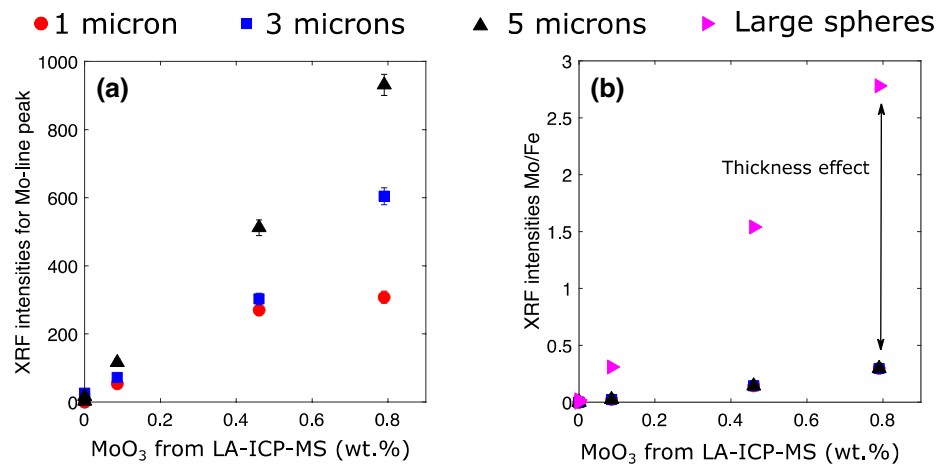
It is possible to calculate the uncertainty (minimum detection limit, MDL) on each measurement i ($C_{MDL,i}$) following Petitgirard et al. (2009) such that:

$$C_{MDL,i} = \frac{3 \times \sqrt{I_B}}{I_i} \times \frac{\sqrt{t}}{\sqrt{1000}} \times C_i \quad (1)$$

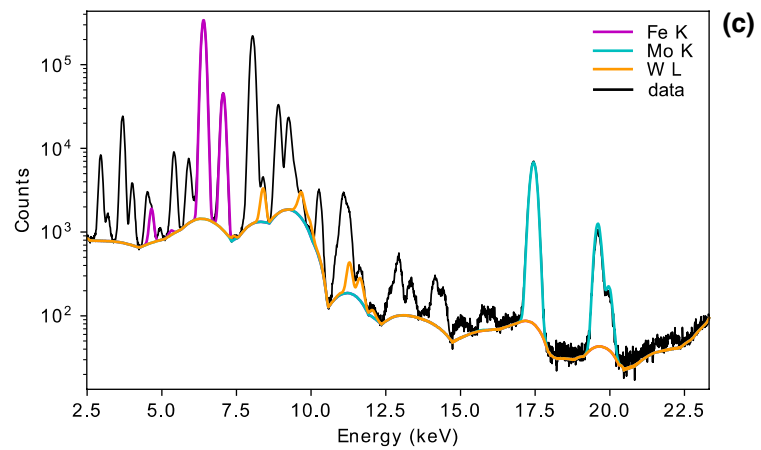
with I_B the intensity of the background, I_i the intensity of the peak of the element i integrated over the 3σ zone, t the collection time, and C_i the actual concentration of element i . Some chemical elements in our standards were present at low concentrations (i.e., 70 ppm of Mo in PO100 for instance). As seen with Fig. 1, it is possible to derive precise calibration curves, that are applicable from very low concentrations to orders of magnitude higher. From this and Eq. 1, we can estimate that the detection limit is a few ppm for elements that can be detected with K-alpha lines, and few tens of ppm for elements with L-lines, which makes nano-XRF an excellent method for resolving low concentrations of elements in FIB-extracted samples. Of course, this depends on the complexity of the sample (textural complexity or non-homogeneous element concentrations for instance), and can vary if the sample is more complex than what we used here. As also discussed below, ideally, the major elements composition of the standard and the sample should be close to increase accuracy.

Additionally, if the thickness of the sample of interest is known, the main parameter that can be tuned and can

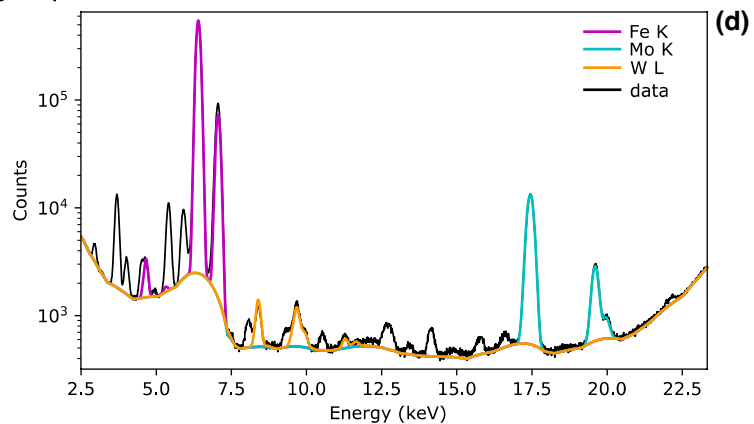
Fig. 1 Effect of thickness on the Mo intensity with **a** 1-, 3- and 5-microns thickness. **b** Effect of thickness on the XRF intensities of Mo/Fe measured from FIB lamellae and large spheres. Impact of thickness on number of counts for **c** a FIB lamella of 3 microns thickness and **d** a large sphere, in both cases for the sample PO100



FIB lamella



Large sphere



influence the output is the density of the sample when using PyMca software. This parameter is not always easily accessible, especially for experimental samples. To estimate the importance of the chosen density on the output results, we changed the estimated density of our FIB lamellae of standard IZ-01 from 2.5 to 3.5 g cm⁻³ while keeping the other parameters constant. The choice of these densities is justified

because the composition of this standard approximates the eutectic composition of the anorthite-diopside system at 1-bar that have respective densities of ~2.7 and ~3.2 g/cm³. We plot in Fig. 2 the result of changing the density compared to the concentrations reported in Chen et al. (2020) for IZ-01. One can see that there is an excellent agreement between what is expected and the concentrations derived

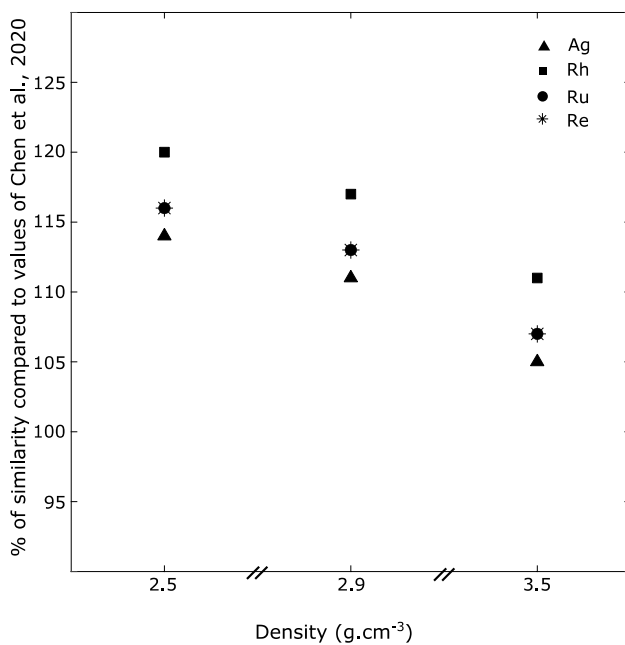


Fig. 2 Percentage of similarity between the values derived from our nano-XRF measurement and the values provided by Chen et al. (2020) for the standard IZ-01 as a function of the density chosen. We calculated the abundances of each element using the software PyMca. A value of 100 on the Y axis means that our calculation from nano-XRF measurements reproduce exactly the value proposed by Chen et al., 2020

using nano-XRF technique, with a maximum difference of 20%. For all elements, using a density of 3.5 g cm^{-3} results in concentrations closest to the expected ones, since there are 10% or less of difference between our results and that provided by Chen et al. (2020). In this case, we used calcium as internal standard because it is one of the major elements of this standard (see Table 1), but Ca can be affected by reabsorption, which may explain the deviation of about 10% from the expected values. Ideally, it would be better to use another element closer to the one of interest, like iron, but in this particular standard, the amount of iron is quite low ($\sim 0.2 \text{ wt}\%$), precluding its usage as reliable internal calibrant.

Further, we could identify several limitations related to the use of nano-XRF with FIB lamellae. First, because of the use of FIB, we could always detect Ga implantation on our standards (and samples), along with Pt signal coming from the welding, and copper from the TEM grid. Hence, if one wants to study one of these three elements, some adjustment has to be made, for example the use of another element than Pt during the FIB procedure. Otherwise, we suspect that no useful information can be extracted from the analysis. We also noted that the way the sample is attached to the Cu grid is of great importance. Indeed, the sample should ideally be welded from both sides, and be aligned with the surface of

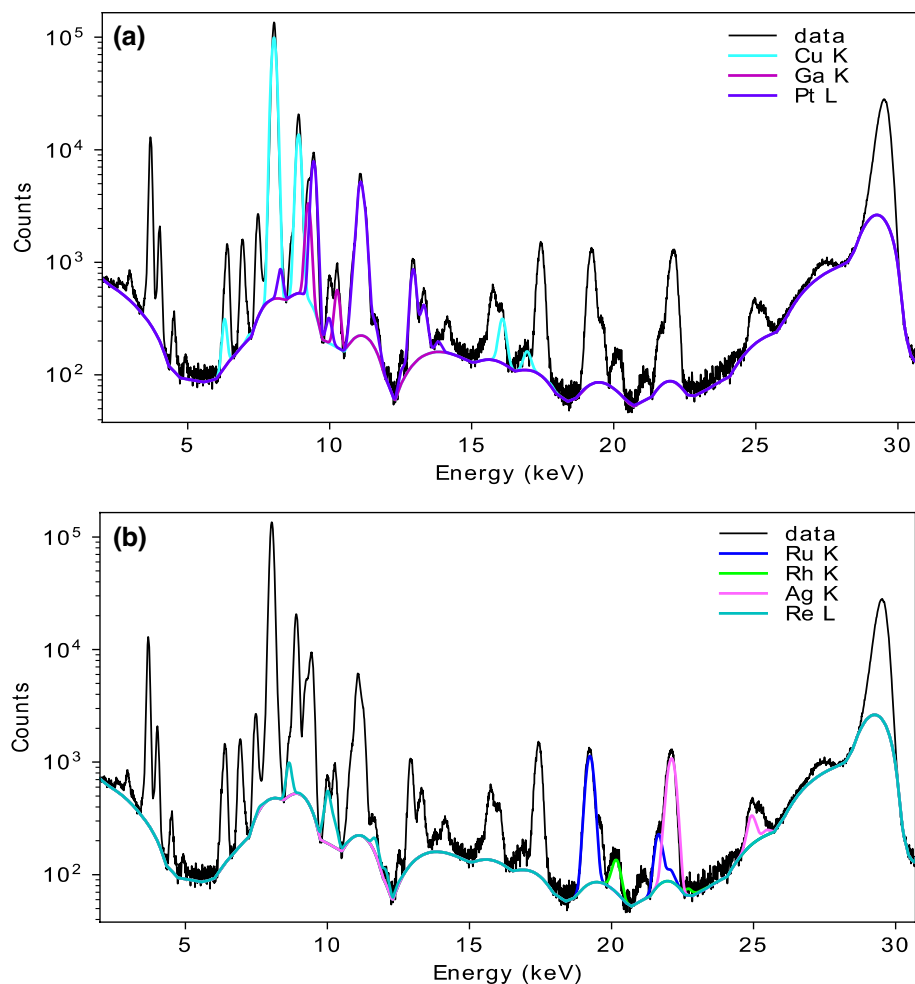
the Cu grid, to maximize the signal coming out and avoid shadow effect on the detector. But regardless of the welding, the fluorescence coming from the Cu-grid will be visible on the spectra, which can be an issue, depending on the elements of interest. We illustrate these effects on Fig. 3 where one can see the intensity of the peaks for Cu, Ga and Pt on our FIB extracted material. Those spectra are from the standard IZ-01, and one can see that there are some overlaps between the peaks of the elements of interest and Cu, Pt and Ga. Welding the sample to a Si-wafer (instead of a Cu-grid and a silicon nitride membrane as we did) has been done in previous studies (Suer et al. 2021) but not tested here. While it sounds like a good alternative, Si-wafer are thick and this might result in scattering that could blind the detectors.

Finally, it is worth noting that the standards should ideally be very close (in composition, structure, density) to the samples. This is important to limit the matrix effect when establishing the calibration lines. In our case, the standards were not synthesized at high pressure, and the composition is not exactly that of the samples. Nonetheless, the use of our standards is justified as these were the most reliable standards available to us. In the future, it would be interesting to test the potential differences that arise from using standards synthesized at high P - T .

NanoSIMS measurements

NanoSIMS relies on using a highly focused primary ion beam (O^- or Cs^+) to bombard the sample and by doing so sputters ionized material from the surface layers. The ejected secondary ions are subsequently analyzed by a mass spectrometer. This technique is optimized for nanoscopic scale spatial resolutions. NanoSIMS measurements are sensitive to matrix effects, so we took particular care in synthesizing and using relevant standards. NanoSIMS analyses were performed using the CAMECA NanoSIMS 50L at the Open University (Milton Keynes, UK). Prior to analysis, an area of each sample was pre-sputtered using a focused primary beam of 16 keV O^- ions with a probe current of $\sim 100 \text{ pA}$ to remove surface contamination and achieve a constant count rate. The sizes of the pre-sputtered areas varied from 15×15 to 20×20 microns. Analyses were then carried out in imaging mode by rastering a 50 pA O^- beam onto the inner 10×10 to 15×15 microns areas. With this probe, a spatial resolution of $\sim 300 \text{ nm}$ was achieved. The mass resolving power was set at > 5000 (Cameca definition) and secondary ions of $^{95}\text{Mo}^{16}\text{O}^+$, $^{186}\text{W}^{16}\text{O}^+$, $^{30}\text{Si}^+$, and $^{54}\text{Fe}^+$ (sometimes $^{56}\text{Fe}^+$) collected in electron multipliers simultaneously. The oxide ions were measured as they offered enhanced secondary ion yields over the atomic ions, especially for W. Final isotope maps are generated by aligning and summing stacks of 100 images, with each image composed of 128×128 pixels with a dwell time of 2 ms per pixel. Total analysis

Fig. 3 Intensity spectra from standard IZ-01 obtained by Nano-XRF. Intensity of **a** the Cu Ga and Pt peaks coming from the TEM grid and the FIB procedure, **b** Ru, Rh, Ag and Re



time for each map is therefore approximately 60 min. The data were processed with L'Image software (Larry Nittler, Carnegie Institute Washington D.C.), correcting for detector deadtime and stage drift, after which we extracted from the region of interest the ratios $^{95}\text{Mo}/^{30}\text{Si}$ and $^{186}\text{W}/^{30}\text{Si}$ for the silicate standard, and $^{95}\text{Mo}/^{54}\text{Fe}$ and $^{186}\text{W}/^{54}\text{Fe}$ for the metallic one. We performed five analyses on each standard to test the reproducibility of the measurements. From these measurements, we derived calibration curves for $^{95}\text{Mo}/^{30}\text{Si}$ and $^{186}\text{W}/^{30}\text{Si}$ ratios in the silicate matrix and $^{95}\text{Mo}/^{54}\text{Fe}$ and $^{186}\text{W}/^{54}\text{Fe}$, see Fig. 4. On those figures, each point is the mean of the five analyses performed on each sample. One can see that for the metallic standards, the calibration curve is slightly less good than for the silicate one. This is probably due to the presence of a dendritic quench texture that developed upon quench for the spheres synthesized using the aerodynamic levitation device.

We display in Fig. 5 the NanoSIMS maps that were established for the standards PO1000 for ^{30}Si , ^{56}Fe , ^{95}Mo and $^{186}\text{W}/^{16}\text{O}$. One can see that at the scale of the measurements, no heterogeneity can be detected in the material, such as nanonuggets. The counts are of course much higher for Si

and Fe, but Mo and W are still detectable with this technique. It must be noted that, contrary to the measurements we did using nano-XRF, the standards were bulk and not extracted by FIB. We did so because NanoSIMS is a technique that is especially sensitive to the surface of the analyzed sample, so it allowed us to save a lot of preparation time.

Application to high P - T samples

High P - T experiments

We applied both nano-XRF and NanoSIMS techniques on samples synthesized using a LH-DAC for which the objective was to evaluate the evolution of the metal-silicate partition coefficient (D , with $D = X_M^{\text{metal}}/X_{\text{MO}_{n/2}}^{\text{silicate}}$ in molar fraction, with n the valence state of the element M) of tungsten and molybdenum with pressure and temperature. To do so, it is necessary to measure trace concentrations of siderophile elements in quenched silicate melt equilibrated at high P - T

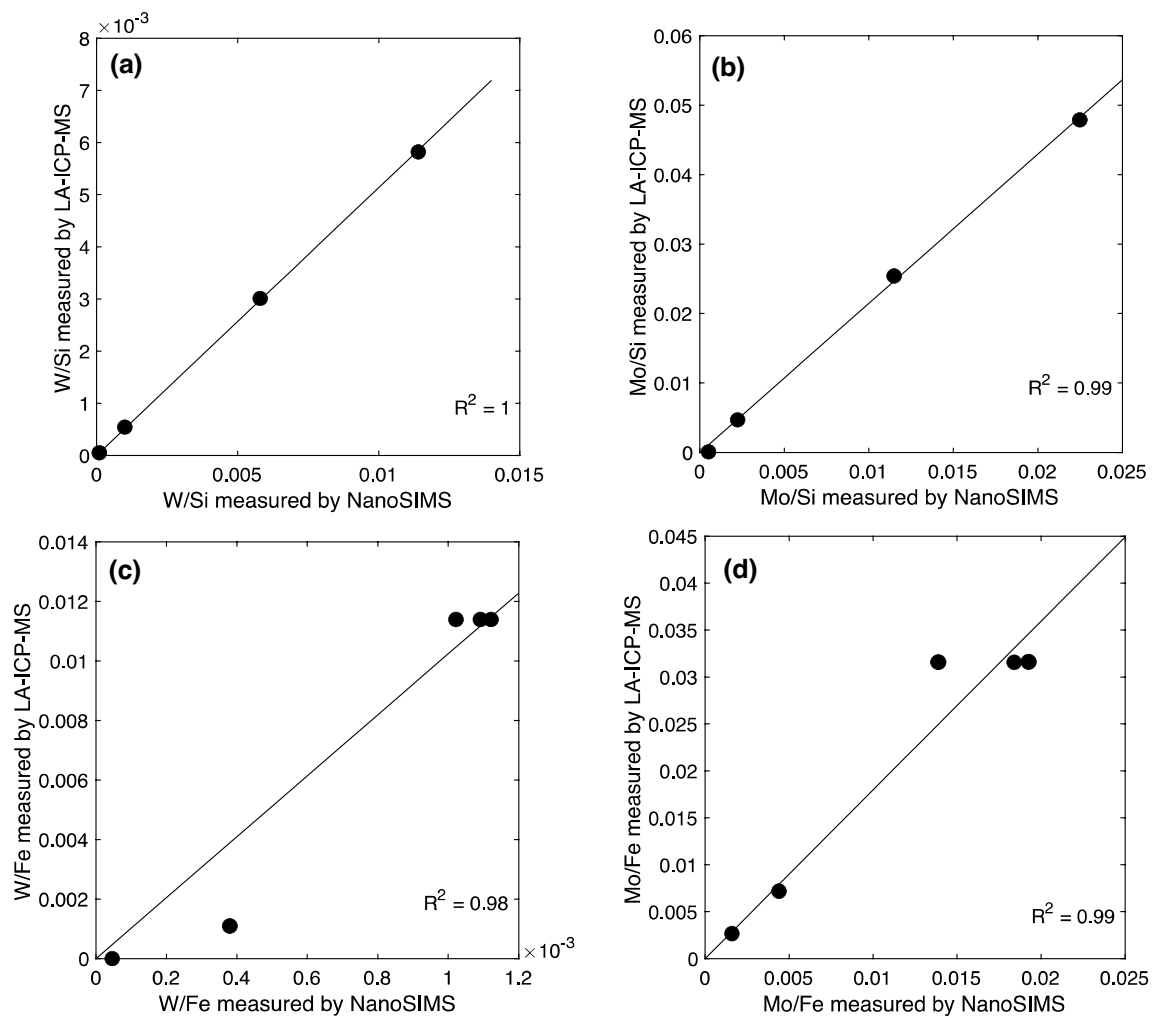


Fig. 4 Calibration curves obtained at the NanoSIMS for **a** W/Si and **b** Mo/Si in silicate melts and for **c** W/Fe and **d** Mo/Fe in metallic melts

with a quenched molten metallic alloy doped in siderophile elements. In our case, we studied the siderophile elements Mo and W. Those two elements are vertically adjacent in the periodic table, and they are the only two MSEs that are cosmochemically refractory. As such, they can be used as tracers of core–mantle differentiation, because they should be present in chondritic proportions in the bulk Earth. In addition, W is part of the Hf–W isotopic system that is used to constrain the timing of core formation (e.g., Kleine et al. 2002).

As starting materials, we used sample PO1 synthesized by aerodynamic levitation as described previously for the silicate part (see also composition in Table 1), and iron–nickel ($\text{Fe}_{95}\text{Ni}_5$) or FeNiS ($\text{Fe}_{80}\text{Ni}_{10}\text{S}_{10}$) thin foils for the metallic part. The choice of the FeNiS alloy was made to test the effect of sulfur on the metal–silicate partitioning of W and Mo. A rhenium gasket with an initial thickness of 250 μm was pre-indented down to 40 μm using diamonds with 200-to-300-micron culets. Subsequently, a hole of

about 100 μm diameter was machined in the center of the indentation, using a laser drill, to serve as a sample chamber. A thin foil of metal alloy sandwiched between two layers of silicate glass starting material was loaded in the sample chamber (Fig. 6). The pressure was slowly increased and monitored using the diamond Raman edge method (Akahama and Kawamura 2004) until the target pressure was reached. The loaded and pressurized diamond anvil cells were then heated to the target temperature using a double-sided YAG laser at BGI and at the GeoForschung Zentrum (GFZ, Potsdam). Details of both heating systems are provided in Lobanov et al. (2020) and Blanchard et al. (2022), respectively. The temperature was monitored using the spectro-radiometric analysis of the thermal emission spectrum of the sample under the gray body assumption (Benedetti and Loubeyre 2004). The peak temperature was maintained for a few seconds, which is enough to closely approach thermodynamic equilibrium given the size of the samples (few tens of microns, see Fig. 6c) and the high temperatures, above the

Fig. 5 NanoSIMS chemical maps of standard PO1000 for several isotopes (^{30}Si , ^{56}Fe , $^{186}\text{W}^{16}\text{O}$ and $^{95}\text{Mo}^{16}\text{O}$)

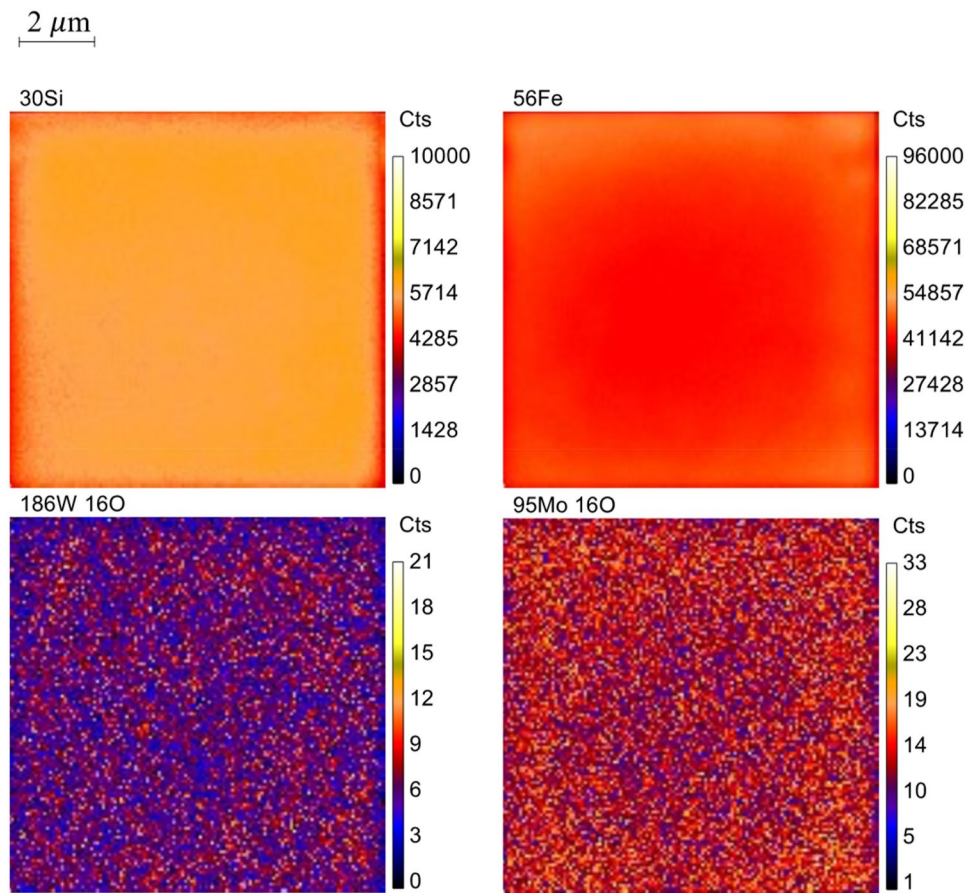
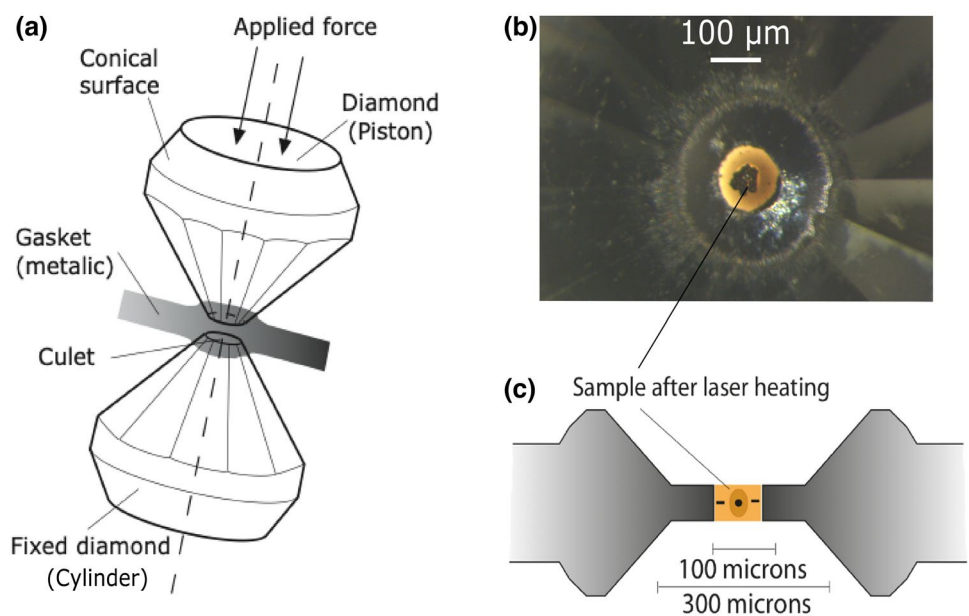


Fig. 6 **a** Schematic drawing of a diamond anvil cell apparatus. **b** Optical picture taken through the diamonds of a loaded diamond anvil cell experiment. **c** Schematic drawing showing the geometry of the sample embedded inside the rhenium gasket, seen from the side



peridotite liquidus (Fiquet et al. 2010). The target peak temperature was chosen at each pressure point so that both the metal and the silicate were molten. Temperatures given in Table 3 are the averages of three to six measurements taken

at the peak temperature. Following Lobanov et al. (2021), we estimate that the uncertainties on the temperature measurement is about 20% relative, and is an upper bound on the error in temperature associated with non-graybody effects.

Table 3 Summary of experimental conditions and metal–silicate partition coefficients (and their associated uncertainties in brackets) retrieved from nano-XRF and NanoSIMS measurements

	P (GPa)	T (K)	D_{Mo}^*	D_{W}^*	$D_{\text{Mo}}^{\#}$	$D_{\text{W}}^{\#}$
×1	25	2630	187 (62)	–	–	–
×2	27	2820	135 (45)	–	–	–
×3	43	3230	82 (27)	–	–	–
×4	46	3330	49 (16)	–	–	–
×5	70	3700	26 (9)	–	–	–
×6	38	2940	142 (47)	60 (20)	–	–
×7	45	3230	116 (39)	37 (12)	–	–
×8	35	2900	112 (37)	32 (11)	70 (15)	25 (5)
×9	63	3850	75 (25)	34 (11)	40 (10)	10 (5)
×10	55	3640	45 (15)	17 (6)	–	–
×11	75	4000	37 (12)	11 (4)	–	–
×12	105	4760	7.5 (2)	2 (1)	–	–

Uncertainties on P and T are estimated to be 5 GPa and 20% of the value displayed, respectively

*Calculated using nano-XRF

#Calculated using NanoSIMS

The laser power was then shut down to ensure a fast quench of the sample and, because the diamonds are excellent thermal conductors, the heat is very quickly dissipated out of the sample, so that the quench is quasi-instantaneous. The samples were recovered at ambient pressure, after slowly decompressing the load on the diamond anvils, to perform ex situ measurements. Given the geometry and very small size of the samples in such experiments, the samples are not directly accessible since the zone that reacted and equilibrated at high P – T is buried below the surface (see Fig. 6c). To extract the region of interest where the peak temperature was reached and the sample had melted, we used the FIB facility at the BGI and at the GFZ, that allowed us to extract 3-micron thick lamellae from each of our experiments (see procedure described in the supplementary information, and Fig. S1). Care was taken to extract lamellae that had parallel surfaces on both sides of the samples for the metal and the silicate phases. The extracted samples had the same thickness as the standards that were used to establish the calibration (3 microns). We present in Table 3 the experimental conditions of the high P – T runs of this study. For these samples, electron microprobe analysis was not performed.

Nano-XRF measurements of high P – T samples

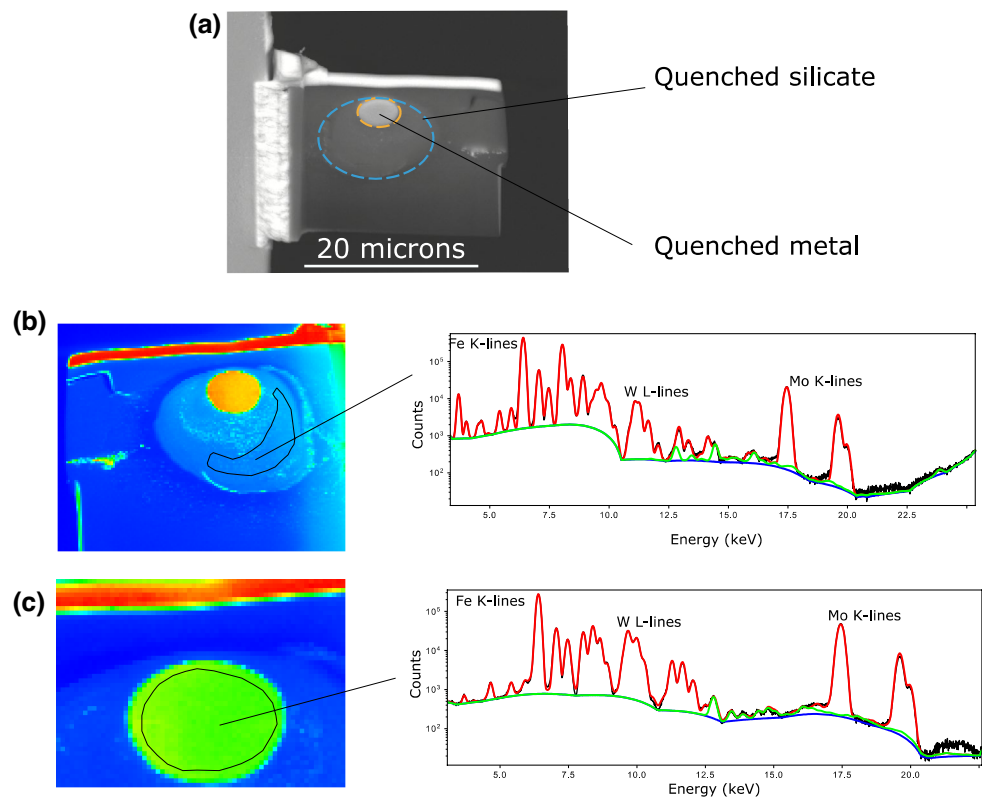
FIB lamellae from the samples were attached to PEEK holders, the same way we fixed standards (see above), to perform nano-XRF analysis. We could produce high resolution maps of the samples using a nanobeam at ID16B as described above. We show in Fig. S3 a nano-XRF intensity map of such a sample that was obtained with an acquisition time of 1000 ms per pixel, the longest that we have performed in this study. One can see the level of detail that can be obtained using such a probe. The spatial resolution that is reached

allows us to observe small features such as the calcium perovskite around the quenched metal that was molten at high P – T . Note that this particular sample does not contain Mo or W, so it was not used to calculate D_{Mo} and D_{W} .

We show in Fig. 7 another typical map that can be obtained using this technique from which we extracted chemical information. Since those samples have two phases present (metal and silicate) as opposed to the standards described above, we had to select the ROIs for each of the phases of sample ×8 synthesized at 35 GPa and 2900 K (see Fig. 7). We could integrate over a large area of sample to have better statistic using the software PyMca. This procedure was performed on each phase of each sample and we could extract Mo/Fe and W/Fe ratios that could be compared with the calibration curve obtained for the standards (see Fig. 1). By doing so, we could calculate the metal–silicate partition coefficients of W (D_{W}) and Mo (D_{Mo}) for our experiments, as presented in Table 3.

We present in Fig. 9, a comparison between a recent determination of D_{W} and D_{Mo} by Huang et al. (2021) and the results derived in this study. Unlike us, the partition coefficients of Huang et al. (2021) were retrieved from electron microprobe analysis. In our case, no electron microprobe analysis was carried on the samples. Our quantification merely relies on the calibration curves presented above. This allows for a direct assessment of the validity of our method, and one can see that the magnitudes of D_{W} and D_{Mo} derived by both studies are comparable. Our study extends the P – T range of metal–silicate partition coefficients for those elements, and it also agrees with the conclusions of Huang et al. (2021) that pressure makes both W and Mo less lithophile (decrease of D with pressure). Nevertheless, the temperature effect seems more controversial, with a decrease of both D_{Mo} and D_{W} with temperature. For Mo, this has already been

Fig. 7 **a** Backscattered electron image of sample $\times 8$ recovered by FIB from LH-DAC experiments. **b** Total intensity map obtained by nano-XRF measurements along with integrated spectra of the delimited area for the silicate and **c** for the metal



proposed by Siebert et al. (2011), whereas such an effect was not proposed for W in previous studies (Siebert et al. 2011; Wade et al. 2012; Huang et al. 2021; Jennings et al. 2021). It must be noted that for previous studies deriving thermodynamic parameterization of evolution of the metal–silicate partition coefficients are not used at face value, but normalized to the metal–silicate partitioning of Fe (D_{Fe}) at the power $n/2$ with n being the valence of the element considered. By doing so, the dependence on oxygen fugacity of the experiment is removed, and this is especially important for high valence elements, such as W and Mo (6+ and 4+ respectively). In this study, we have not attempted to calculate D_{Fe} or to proceed with thermodynamic modeling, but we were rather interested in testing the two analytical techniques on a suite of standards and high P – T samples.

For the standards, we had EPMA analysis that allowed us to use a known matrix correction to estimate the concentration of the elements of interest. In the case of our high P – T samples, this can also be done, but several difficulties have to be overcome. To perform EPMA analysis on FIB-recovered samples, it is necessary to have phases that are large enough to accommodate the interaction volume produced by the electron beam (about 1 micron^3 with operating conditions of 15–20 keV). Hence, it is mandatory to have phases of at least several microns thick to perform accurate EPMA analysis. Another complexity is to move high P – T samples from one holder to another without losing them, since those

samples are extremely small, fragile and easy to lose, even when attached to a TEM Cu grid. If these difficulties can be overcome, then it is possible to analyze trace elements, as we did for standards in addition to the major elements using conventional probes. Here, we did not perform EPMA measurements on our high P – T samples.

Another potential limiting factor in our case is the difference in the composition of our standards compared to our experimental samples, especially in terms of the iron concentration in the silicate (and to a lesser extent in the metal). Metal–silicate partitioning samples synthesized by LH-DAC have usually up to 20 wt% FeO in the silicate phase (e.g. Siebert et al. 2012; Blanchard et al. 2017; Jackson et al. 2018). This is about twice of what we have in our standards. This ultimately is a source of uncertainties in the values of D_{W} and D_{Mo} that we calculated. Hence, we have estimated a maximum value by directly using the calibration curve, and a minimum value that is half of it to incorporate the factor two difference in FeO between the standards and the sample. The values and their uncertainties reported in Table 3 and Fig. 9 are the result of this treatment.

NanoSIMS measurements of high P – T samples

Two of the high P – T samples were measured using the NanoSIMS: samples $\times 8$ and $\times 9$ synthesized at 35 GPa and 2900 K and 68 GPa and 3850 K, respectively. They were

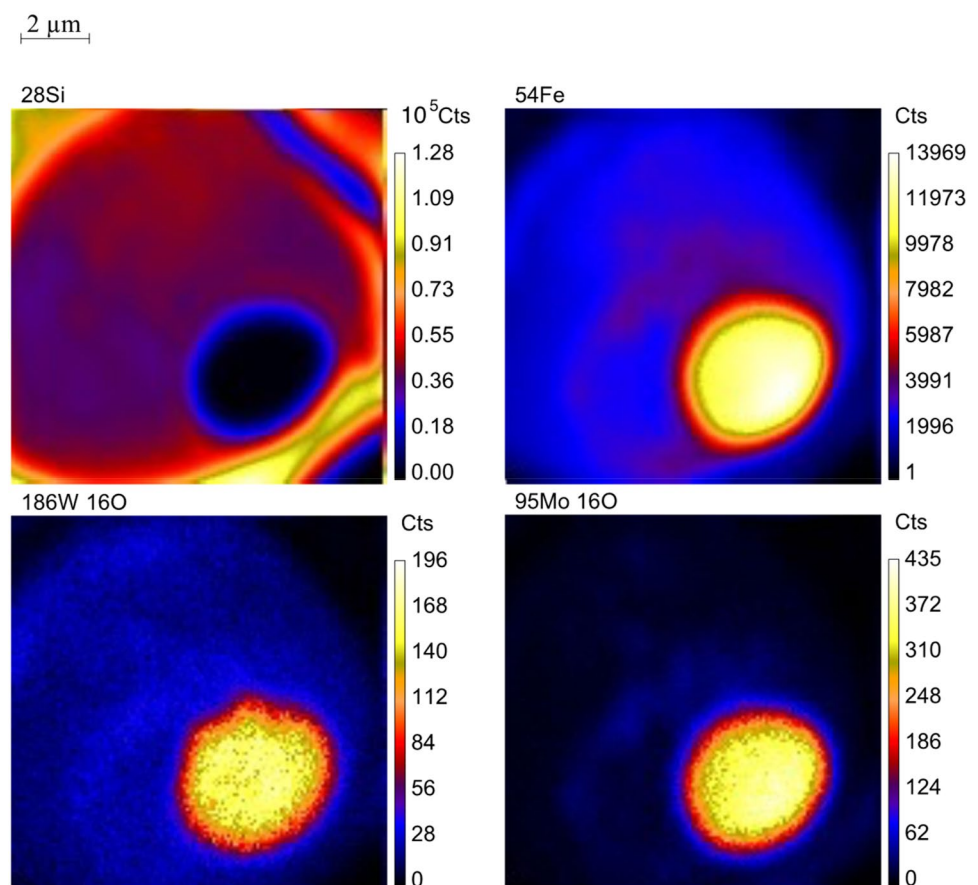
mounted on electrically conductive carbon tape to provide a uniform electric field over the sample. In Fig. 8, the NanoSIMS maps for different isotopic ratios are reported for sample $\times 8$ synthesized at 35 GPa and 2900 K that was already presented in Fig. 7. We first sputtered away the upper layer of each sample to get rid of the oxide layer present at the surface. The O^- anions beam was then scanned across the sample to obtain an overview of the whole samples before selecting specific ROIs for both metal and silicate parts. As for the standards, we could define ROIs in both the metal and the silicate and extract $^{95}\text{Mo}/^{30}\text{Si}$ and $^{186}\text{W}/^{30}\text{Si}$ for the silicate part (excluding the Ni/Si rich area to avoid nanonuggets), and $^{95}\text{Mo}/^{54}\text{Fe}$ and $^{186}\text{W}/^{54}\text{Fe}$ for the metallic part.

Using those ratios and the calibration lines defined earlier, we calculated D_{Mo} and D_{W} for these two samples. The values are given in Table 3, and also reported in Fig. 9. One can see that they compare well with data obtained with nano-XRF and EPMA from Huang et al. (2021). The standards used to calculate D_{Mo} and D_{W} from NanoSIMS measurements are the same as the ones used for nano-XRF. Hence, the same problem arose regarding the difference in composition (mostly in FeO) between our samples and the standards. The uncertainties reported in Table 3 and Fig. 9 are due to this matrix effect.

Conclusions

We have shown that using nanoprobe on samples retrieved using FIB, such as high pressure and high temperature samples synthesized in a LH-DAC, trace element mapping and quantification can be successfully performed. We have compared two nano probes, namely nano-XRF and NanoSIMS, that present some similitudes but also several differences, as summarized in Table 4, that must be taken into account depending on the type of measurements one wants to perform. The spatial resolution of both nano-XRF and NanoSIMS enables analyzing very small structures present in FIB-extracted samples. In this work, we have used both NanoSIMS and nano-XRF to estimate metal-silicate partition coefficients of Mo and W in samples synthesized in laser-heated diamond anvil cells and retrieved by FIB. We obtained results that are comparable to those obtained independently using EPMA. This highlights that these methods are robust, and are suitable for such kind of samples. The elemental sensitivity of those instruments can be used to infer very low concentrations of elements (down to few ppm), as evidenced the detection limits established from the

Fig. 8 NanoSIMS chemical maps of sample $\times 8$ for several isotopes (^{28}Si , ^{54}Fe , $^{186}\text{W}^{16}\text{O}$ and $^{95}\text{Mo}^{16}\text{O}$)



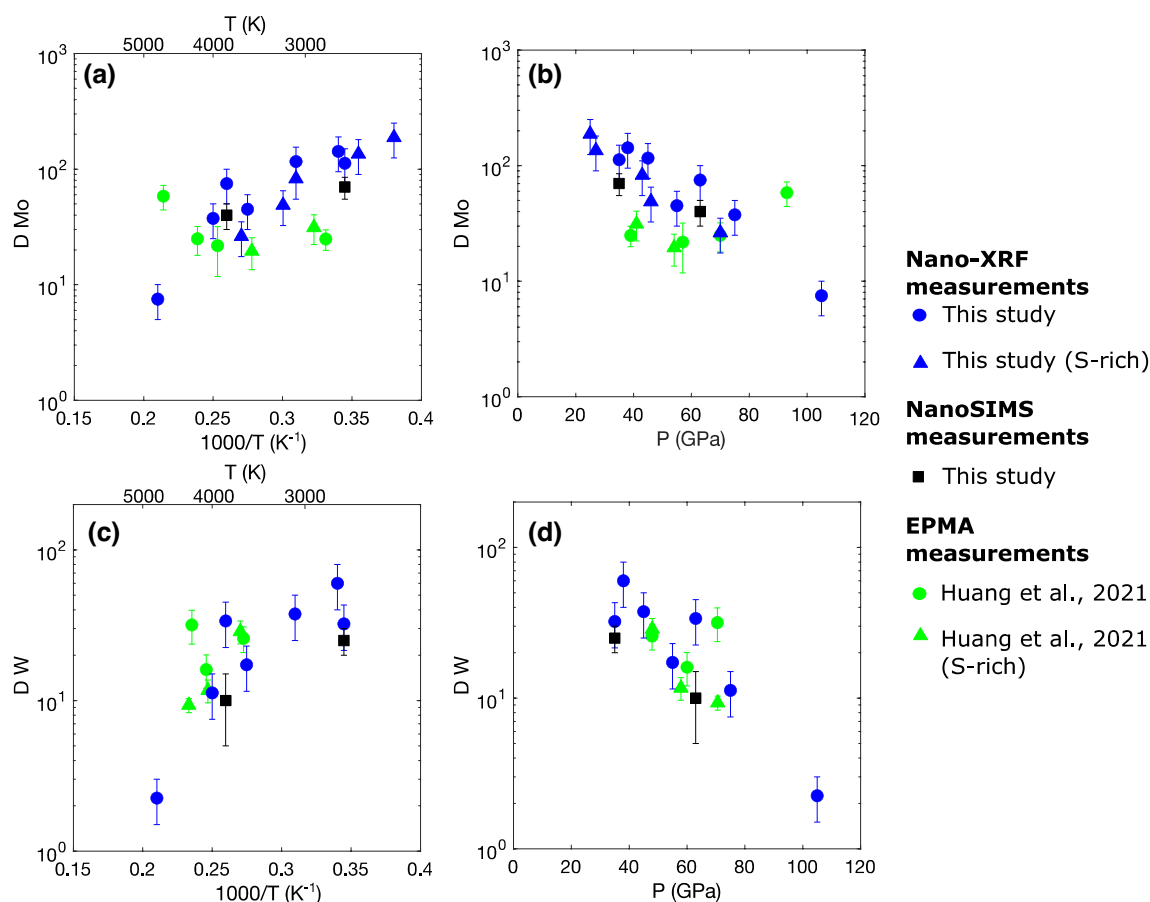


Fig. 9 Comparison between our metal–silicate partitioning coefficient of Mo and W obtained by nano-XRF measurements (in green), and with NanoSIMS measurements (in black) with published data from

Huang et al. (2021) obtained by electron microprobe measurements. The uncertainties on P and T are estimated to be 5 GPa and 20% of each temperature measurement, respectively

Table 4 Comparison of nano-XRF and NanoSIMS analytical techniques

	Nano-XRF technique	NanoSIMS technique
Probe	High energy photon beam	Ion beam (Cs^+ or O^-)
Energy	8–29.5 keV	16 keV
Destructiveness	No	Yes
Element range	From Na to U	From H to U
Sensitive to geometry	Yes	Yes
Isotopic resolution	No	Yes
Sample environment	Atmospheric pressure	High vacuum
Sample preparation	Flat sample fixed on holder	Sample must be coated and flat

study of our standards. Further, the spatial resolutions of 300 nm for the nanoSIMS down to 50 nm (even 10 nm in some cases) for the XRF are promising for the analysis of extremely small samples. Such features are greatly superior to the detection limits and spatial resolution of the microprobe for example. Hence, those methods have a high potential to investigate the behavior of highly siderophile elements in silicate melts, for instance in the frame

of Earth's core-mantle differentiation. More generally, elemental diffusion between grain boundaries of minerals or the partitioning of trace elements between solid–solid or solid–liquid phases can be explored, for example to understand their behavior in the frame of magma ocean solidification.

Supplementary Information The online version contains supplementary material available at <https://doi.org/10.1007/s00269-022-01193-7>.

Acknowledgements We thank Anja Schreiber who performed the FIB at GFZ. Andreas Audéat is thanked for his help and expertise for the LA-ICP-MS measurements. Severine Brassamin is thanked for her help with the levitation apparatus at CEMHTI. IB acknowledges funding from DFG project BL 1690/1-1 and ESRF projects ES-234 and ES-998. The Scios FIB at BGI was financed by DFG Grant INST 91/315-1 FUGG. SP has received support from the European Union's Horizon 2020 research and innovation program to access the Open University NanoSIMS facility at Milton Keynes, UK. Europlanet 2020 RI has received funding from the European Union's Horizon 2020 research and innovation program under grant agreement No 654208. S. S. L. acknowledges the support of the Helmholtz Young Investigators Group CLEAR (VH-NG-1325). WM thanks BMBF project 05K19IP2. We want to thank Oliver Lord and an anonymous reviewer for their reviews, and Stella Chariton for handling our manuscript.

Funding Open Access funding enabled and organized by Projekt DEAL.

Open Access This article is licensed under a Creative Commons Attribution 4.0 International License, which permits use, sharing, adaptation, distribution and reproduction in any medium or format, as long as you give appropriate credit to the original author(s) and the source, provide a link to the Creative Commons licence, and indicate if changes were made. The images or other third party material in this article are included in the article's Creative Commons licence, unless indicated otherwise in a credit line to the material. If material is not included in the article's Creative Commons licence and your intended use is not permitted by statutory regulation or exceeds the permitted use, you will need to obtain permission directly from the copyright holder. To view a copy of this licence, visit <http://creativecommons.org/licenses/by/4.0/>.

References

- Akahama Y, Kawamura H (2004) High-pressure Raman spectroscopy of diamond anvils to 250 GPa: method for pressure determination in the multimegabar pressure range. *J Appl Phys* 96:3748–3751
- Andraut D, Petitgirard S, Lo Nigro G et al (2012) Solid-liquid iron partitioning in Earth's deep mantle. *Nature* 487:354–357. <https://doi.org/10.1038/nature11294>
- Auzende A-L, Gillot J, Coquet A et al (2011) Synthesis of amorphous MgO-rich peridotitic starting material for laser-heated diamond anvil cell experiments—application to iron partitioning in the mantle. *High Press Res* 31:199–213
- Badro J, Ryerson FJ, Weber PK et al (2007) Chemical imaging with NanoSIMS: a window into deep-Earth geochemistry. *Earth Planet Sci Lett* 262:543–551. <https://doi.org/10.1016/j.epsl.2007.08.007>
- Beckhoff B, Kanngießner B, Langhoff N, Wedell R, Wolff H (eds) (2007) Handbook of practical X-ray fluorescence analysis. Springer
- Benedetti LR, Loubeyre P (2004) Temperature gradients, wavelength-dependent emissivity, and accuracy of high and very-high temperatures measured in the laser-heated diamond cell. *High Press Res* 24:423–445
- Blanchard I, Siebert J, Borensztajn S, Badro J (2017) The solubility of heat-producing elements in Earth's core. *Geochemical Perspect Lett*. <https://doi.org/10.7185/geochemlet.1737>
- Blanchard I, Rubie DC, Jennings ES et al (2022) The metal–silicate partitioning of carbon during Earth's accretion and its distribution in the early solar system. *Earth Planet Sci Lett* 580:117374. <https://doi.org/10.1016/j.epsl.2022.117374>
- Bouhifd MA, Jephcoat AP (2011) Convergence of Ni and Co metal–silicate partition coefficients in the deep magma-ocean and coupled silicon-oxygen solubility in iron melts at high pressures. *Earth Planet Sci Lett* 307:341–348. <https://doi.org/10.1016/j.epsl.2011.05.006>
- Brenan JM, McDonough WF, Dalpé C (2003) Experimental constraints on the partitioning of rhenium and some platinum-group elements between olivine and silicate melt. *Earth Planet Sci Lett*. [https://doi.org/10.1016/S0012-821X\(03\)00234-6](https://doi.org/10.1016/S0012-821X(03)00234-6)
- Chen J, Mallmann G, Zhukova I, O'Neill H (2020) Development of PGE-bearing silicate glass standards for quantitative trace element analysis in silicate-based metallurgical slags. *J Sustain Metall* 6:691–699. <https://doi.org/10.1007/s40831-020-00308-0>
- Chou C, Shaw DM, Crocker JH, et al (1983) Siderophile trace elements in the Earth's oceanic crust and upper mantle. *J Geophys Res*
- Ertel W, Dingwell DB, Sylvester PJ (2008) Siderophile elements in silicate melts—a review of the mechanically assisted equilibration technique and the nanonugget issue. *Chem Geol* 248:119–139. <https://doi.org/10.1016/j.chemgeo.2007.12.013>
- Fiquet G, Auzende AL, Siebert J et al (2010) Melting of peridotite to 140 gigapascals. *Science* (80-) 329:1516–1518
- Fischer RA, Cottrell E, Hauri E et al (2020) The carbon content of Earth and its core. *Proc Natl Acad Sci USA* 117:8743–8749. <https://doi.org/10.1073/pnas.1919930117>
- Heinen BJ, Drewitt JWE, Walter MJ et al (2021) Internal resistive heating of non-metallic samples to 3000 K and >60 GPa in the diamond anvil cell. *Rev Sci Instrum*. <https://doi.org/10.1063/5.0038917>
- Huang D, Siebert J, Badro J (2021) High pressure partitioning behavior of Mo and W and late sulfur delivery during Earth's core formation. *Geochim Cosmochim Acta* 310:19–31. <https://doi.org/10.1016/j.gca.2021.06.031>
- Irifune T, Isshiki M, Sakamoto S (2005) Transmission electron microscope observation of the high-pressure form of magnesite retrieved from laser heated diamond anvil cell. *Earth Planet Sci Lett* 239:98–105. <https://doi.org/10.1016/j.epsl.2005.05.043>
- Jackson CRM, Bennett NR, Du Z et al (2018) Early episodes of high-pressure core formation preserved in plume mantle. *Nature* 553:491–495. <https://doi.org/10.1038/nature25446>
- Jennings ES, Jacobson SA, Rubie DC et al (2021) Metal – silicate partitioning of W and Mo and the role of carbon in controlling their abundances in the Bulk Silicate Earth. *Geochim Cosmochim Acta* 293:40–69. <https://doi.org/10.1016/j.gca.2020.09.035>
- Kimura K, Lewis RS, Anders E (1974) Distribution of gold and rhenium between nickel-iron and silicate melts: implications for the abundance of siderophile elements on the Earth and Moon. *Geochim Cosmochim Acta* 38:683–701
- Kleine T, Münker C, Mezger K, Palme H (2002) Rapid accretion and early core formation on asteroids and the terrestrial planets from Hf–W chronometry. *Nature* 418:952–955
- Laurenz V, Rubie DC, Frost DJ, Vogel AK (2016) The importance of sulfur for the behavior of highly-siderophile elements during Earth's differentiation. *Geochim Cosmochim Acta* 194:123–138. <https://doi.org/10.1016/j.gca.2016.08.012>
- Lemelle L, Simionovici A, Schoonjans T et al (2017) Analytical requirements for quantitative X-ray fluorescence nano-imaging of metal traces in solid samples. *Trends Anal Chem*. <https://doi.org/10.1016/j.trac.2017.03.008>
- Li J, Agee CB (1996) Geochemistry of mantle-core differentiation at high pressure. *Nature* 381:686–689. <https://doi.org/10.1038/381686a0>
- Lobanov SS, Schifferle L, Schulz R (2020) Gated detection of super-continuum pulses enables optical probing of solid and molten silicates at extreme pressure-temperature conditions. *Rev Sci Instrum*. <https://doi.org/10.1063/5.0004590>
- Lobanov SS, Speziale S, Brune S (2021) Modelling Mie scattering in pyrolite in the laser-heated diamond anvil cell: Implications

- for the core-mantle boundary temperature determination. *Phys Earth Planet Inter* 318:106773. <https://doi.org/10.1016/j.pepi.2021.106773>
- Mann U, Frost DJ, Rubie DC et al (2012) Partitioning of Ru, Rh, Pd, Re, Ir and Pt between liquid metal and silicate at high pressures and high temperatures—implications for the origin of highly siderophile element concentrations in the Earth's mantle. *Geochim Cosmochim Acta* 84:593–613
- Médard E, Schmidt MW, Wälle M et al (2015) Platinum partitioning between metal and silicate melts: core formation, late veneer and the nanonuggets issue. *Geochim Cosmochim Acta* 162:183–201
- Miyahara M, Sakai T, Ohtani E et al (2008) Application of FIB system to ultra-high-pressure Earth science. *J Mineral Petrol Sci* 103:88–93. <https://doi.org/10.2465/jmps.070612b>
- Palme H, O'Neill HSC (2014) Cosmochemical estimates of mantle composition. In: *Treatise on geochemistry*, 2nd edn. Elsevier Ltd., pp 1–39
- Petitgirard S, Daniel I, Dabin Y et al (2009) A diamond anvil cell for x-ray fluorescence measurements of trace elements in fluids at high pressure and high temperature. *Rev Sci Instrum* 80:1–6. <https://doi.org/10.1063/1.3100202>
- Petitgirard S, Borchert M, Andraut D et al (2012) An in situ approach to study trace element partitioning in the laser heated diamond anvil cell. *Rev Sci Instrum* 83:1–5. <https://doi.org/10.1063/1.3680573>
- Ricolleau A, Fiquet G, Addad A et al (2008) Analytical transmission electron microscopy study of a natural MORB sample assemblage transformed at high pressure and high temperature. *Am Mineral* 93:144–153. <https://doi.org/10.2138/am.2008.2532>
- Rubie DC, Jacobson SA, Morbidelli A et al (2015a) Accretion and differentiation of the terrestrial planets with implications for the compositions of early-formed Solar System bodies and accretion of water. *Icarus* 248:89–108
- Rubie DC, Nimmo F, Melosh HJ (2015b) Formation of the earth's core. In: Gerald Schubert (editor-in-chief) *treatise on geophysics* vol. 9: Evolution of the earth, 2nd edn. Elsevier B.V., pp 43–79
- Rubie DC, Laurenz V, Jacobson SA et al (2016) Highly siderophile elements were stripped from Earth's mantle by iron sulfide segregation. *Science* (80-) 353:1141–1144. <https://doi.org/10.1126/science.aaf6919>
- Shen G, Mao HK (2017) High-pressure studies with x-rays using diamond anvil cells. *Reports Prog Phys*. <https://doi.org/10.1088/1361-6633/80/1/016101>
- Siebert J, Corgne A, Ryerson FJ (2011) Systematics of metal–silicate partitioning for many siderophile elements applied to Earth's core formation. *Geochim Cosmochim Acta* 75:1451–1489
- Siebert J, Badro J, Antonangeli D, Ryerson FJ (2012) Metal–silicate partitioning of Ni and Co in a deep magma ocean. *Earth Planet Sci Lett* 321–322:189–197. <https://doi.org/10.1016/j.epsl.2012.01.013>
- Siebert J, Badro J, Antonangeli D, Ryerson FJ (2013) Terrestrial accretion under oxidizing conditions. *Science* 339:1194–1197. <https://doi.org/10.1126/science.1227923>
- Solé VA, Papillon E, Cotte M et al (2007) A multiplatform code for the analysis of energy-dispersive X-ray fluorescence spectra. *Spectrochim Acta—Part B at Spectrosc* 62:63–68. <https://doi.org/10.1016/j.sab.2006.12.002>
- Suer T-A, Siebert J, Remusat L et al (2021) Reconciling metal–silicate partitioning and late accretion in the Earth. *Nat Commun*. <https://doi.org/10.1038/s41467-021-23137-5>
- Wade J, Wood BJ, Tuff J (2012) Metal–silicate partitioning of Mo and W at high pressures and temperatures: evidence for late accretion of sulphur to the Earth. *Geochim Cosmochim Acta* 85:58–74
- Walker RJ (2009) Highly siderophile elements in the Earth, Moon and Mars: update and implications for planetary accretion and differentiation. *Chem Erde-Geochem* 69:101–125

Publisher's Note Springer Nature remains neutral with regard to jurisdictional claims in published maps and institutional affiliations.